Advanced Deep Learning Approaches for Fault Detection and Diagnosis in Inverter-Driven PMSM Systems

Abdelkabir BACHA[1], Ramzi El IDRISSI[2], Fatima LMAI[3],
Hicham EL HASSANI[4], Khalid Janati Idrissi[5], Jamal BENHRA[6]
OSIL Team-LARILE Laboratory-School of Electrical and Mechanical Engineering,
Hassan II University of Casablanca, Casablanca, Morocco[1,4,6]
LPMAT-Physics Department-Faculté des Sciences AIN CHOCK, Hassan II University of Casablanca, Casablanca, Morocco[2,3]
Mechanical Engineering Team-Laboratory: Mechanical Engineering-Faculty of Sciences and Technology of Fez,
Sidi Mohamed Ben Abdellah University of Fez, Fez, Morocco[5]

***Abstract*—This paper presents a comprehensive approach to fault detection and diagnosis (FDD) in inverter-driven Permanent Magnet Synchronous Motor (PMSM) systems through the innovative integration of transformer-based architectures with physics-informed neural networks (PINNs). The methodology addresses critical challenges in power electronics reliability by incorporating domain-specific physical constraints into the learning process, enabling both high accuracy and physically consistent predictions. The proposed system combines advanced sensor fusion techniques with real-time monitoring capabilities, processing multiple input streams including phase currents, temperatures, and voltage measurements. The architecture's dual-objective optimization approach balances traditional classification metrics with physics-based constraints, ensuring predictions align with fundamental electromagnetic and thermal principles. Experimental validation using a comprehensive dataset of 10,892 samples across nine distinct fault scenarios demonstrates the system's exceptional performance, achieving 98.57% classification accuracy while maintaining physical consistency scores above 0.98. The model exhibits robust performance across varying operational conditions, including speed variations (97.45-98.57% accuracy range) and load fluctuations (97.91-98.12% accuracy range). Notable achievements include perfect detection rates for certain critical faults, such as high-side short circuits and thermal anomalies, with area under ROC curve (AUC) scores of 1.0. This research establishes new benchmarks in condition monitoring and fault diagnosis for power electronic systems, offering practical implications for predictive maintenance and system reliability enhancement.**

Keywords*—Fault detection and diagnosis; PMSM; deep learning; transformers; physics-informed neural networks; power electronics

I. Introduction

The increasing deployment of Permanent Magnet Synchronous Motors (PMSMs) in critical applications, from electric vehicles to industrial automation, has created an urgent need for reliable and interpretable fault detection systems [1], [2]. While traditional machine learning approaches have demonstrated potential in this domain [3], significant challenges persist that limit their practical effectiveness. A primary concern is the lack of physical consistency in predictions, which can lead to unrealistic fault diagnoses that compromise system reliability. Deep learning models, despite their computational power, often suffer from limited interpretability, which significantly reduces trust in their decision-making capabilities in critical situations. Furthermore, these approaches frequently demonstrate insufficient robustness to variations in operating conditions and noise, making them less reliable in real-world industrial environments.

A fundamental limitation of current approaches lies in their inability to effectively leverage domain knowledge within the learning process. This deficiency, combined with high false alarm rates in traditional data-driven approaches, creates significant barriers to practical implementation. These limitations become particularly problematic in safety-critical applications where incorrect fault diagnoses could lead to catastrophic failures, resulting in substantial economic losses or safety risks.

Previous attempts to address these challenges have primarily focused on either pure data-driven approaches or model-based methods, failing to effectively combine the advantages of both paradigms. Model-based approaches, while theoretically sound, often struggle with complex, nonlinear fault dynamics that characterize real-world PMSM operations. Conversely, pure data-driven methods, though capable of handling complex patterns, may violate fundamental physical constraints that govern motor behavior. Traditional hybrid approaches have attempted to bridge this gap but lack a systematic framework for integrating domain knowledge with learning algorithms.

This research addresses these fundamental challenges through the development of a novel physics-informed deep learning architecture. The proposed approach systematically integrates domain knowledge with advanced neural network capabilities, creating a robust framework that maintains physical consistency while leveraging the pattern recognition capabilities of deep learning. This integration represents a significant step forward in creating reliable, interpretable, and physically consistent fault detection systems for PMSM applications.

A. Background and Motivation

Recent advancements in deep learning have revolutionized fault detection in power electronic systems [4], [5]. However, conventional neural networks treat the problem as a pure data-fitting exercise, potentially leading to physically inconsistent

predictions [6]. The incorporation of physics-based constraints through PINNs offers a promising solution to this limitation.

B. Research Objectives

The primary objectives of this study are:

- To develop and implement a PINN architecture specifically designed for PMSM fault detection
- To compare the performance of PINNs with traditional machine learning classifiers
- To analyze the impact of physics-based constraints on model robustness and generalization

The complete dataset has been published in the Zenodo repository [7] under DOI: 10.5281/zenodo.13974503. Additionally, comprehensive documentation and source code are available as open-source materials on the authors' GitHub profile [8]. The repository includes detailed methodology for thermistor calibration.

II. Literature Review

A. Traditional FDD Methods

Early approaches to fault detection in PMSM systems primarily relied on model-based methods and signal processing techniques. Model-based approaches typically utilize mathematical models of the PMSM system to generate residuals between the predicted and measured signals [6], [9]. Signal processing methods, such as Fast Fourier Transform (FFT) and wavelet analysis, have been widely used for extracting fault-related features from motor current and voltage signatures [5], [10].

B. Power Electronics Reliability and Fault Mechanisms

Understanding the fundamental reliability aspects of power electronic converters is crucial for effective fault detection. Recent studies have established comprehensive guidelines for reliability prediction [11] and investigated specific fault mechanisms in inverter systems [12]. Particular attention has been given to switch faults in power electronic converters [13], which represent one of the most common failure modes in PMSM drive systems.

C. Thermal Considerations in FDD

Thermal analysis has emerged as a critical aspect of fault detection in power electronic components [14]. Temperature monitoring of inverter components provides valuable information for early fault detection and prevention of catastrophic failures. Recent studies have demonstrated the effectiveness of integrated thermal and electrical monitoring approaches [15].

D. Machine Learning in FDD

The application of machine learning to FDD has evolved significantly over the past decade [16]. Initial approaches used traditional machine learning algorithms such as Support Vector Machines (SVM) and Random Forests for fault classification. These methods demonstrated improved performance compared to conventional techniques but still relied heavily on manual feature engineering [3], [17]. The integration of machine learning with condition monitoring systems has shown particular promise in industrial applications [18].

E. Deep Learning Advances

Recent years have seen a surge in deep learning applications for FDD. Convolutional Neural Networks (CNNs) and Recurrent Neural Networks (RNNs) have shown promising results in automatic feature extraction and temporal pattern recognition [19], [20]. However, these approaches often lack the ability to incorporate domain knowledge and physical constraints of the PMSM system [14]. Notably, hybrid approaches combining model-based and data-driven methods have emerged as a promising direction [21].

F. Real-Time Implementation Considerations

The practical implementation of FDD systems presents unique challenges, particularly in real-time applications [22]. Recent work has focused on developing efficient algorithms suitable for embedded systems and microcontroller implementation [23], [24]. These implementations must balance computational efficiency with detection accuracy while maintaining robustness against noise and system variations [25].

III. Experimental Setup Overview

The experimental setup consists of four main subsystems: power electronics inverter, permanent magnet synchronous motor (PMSM), control system, and data acquisition system, see Fig. 1. The setup was designed to enable comprehensive fault simulation and data collection under various operating conditions.

A. Power Electronics Inverter

1) Main components: The power electronics inverter design incorporates modern reliability considerations [12], [13] and follows established fault detection approaches [14], [15], [21].

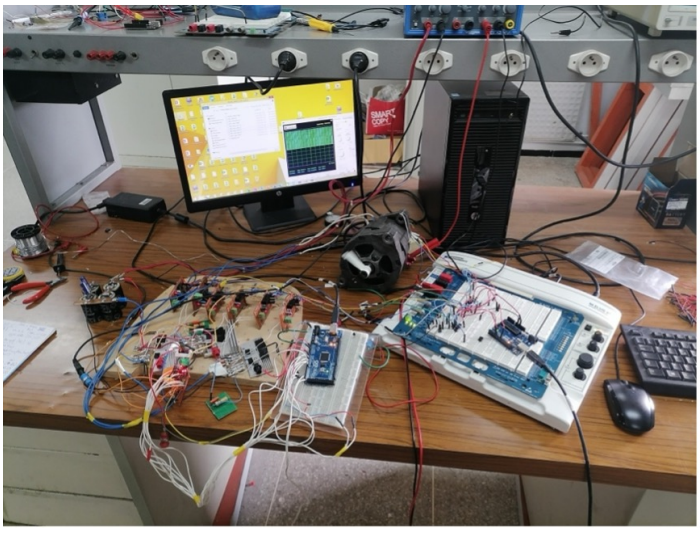

Fig. 1. A picture of the experimental setup.

The power electronics hardware architecture comprises several key components integrated to ensure robust and reliable operation. The system is powered by a 15V DC input voltage source, which feeds into a sophisticated power stage featuring six IRF1404N MOSFETs strategically arranged in three half-bridge configurations. These switching devices are controlled through HCPL3120 gate drivers, selected for their superior isolation characteristics and robust driving capabilities. To maintain stable DC bus voltage and minimize ripple, the DC link incorporates a substantial 2200 μF capacitor bank. Voltage transients and switching spikes are effectively suppressed through the implementation of two RC snubber circuits, each consisting of a 10 Ω resistor in series with a 2.2 nF capacitor.

The design incorporates comprehensive protection features to ensure safe and reliable operation. Galvanic isolation between the control and power circuits is achieved through the gate drivers' built-in isolation barriers, significantly enhancing system safety and noise immunity. Voltage regulation is maintained through a B1215S-2W isolated DC/DC module, which provides stable 15V supply for both the gate drivers and the high-side floating power supplies. Electromagnetic Interference (EMI) is effectively mitigated through strategically placed snubber circuits connected to the DC bus terminals, ensuring clean switching waveforms and reduced electromagnetic emissions. This integrated approach to protection and power quality management ensures optimal system performance while maintaining high reliability standards. Table I provides a synthesis of the Power Electronics Hardware Specifications.

TABLE I. POWER ELECTRONICS HARDWARE SPECIFICATIONS

Component	Model/Specification	Key Characteristics
Power Stage Components		
Power Supply	DC Input	• Input voltage: 15V DC • Current rating: 10A max
MOSFETs	IRF1404N	• V_{DS}: 40V • $R_{DS(on)}$: 4mΩ • I_D: 202A • Configuration: 3 half-bridges
Gate Drivers	HCPL3120	• Peak output current: 2.5A • Propagation delay: 0.5μs • CMR: 15kV/μs • Isolation: 3750V$_{rms}$
DC Link Capacitor	Electrolytic	• Capacitance: 2200μF • Voltage rating: 35V • ESR: 0.05Ω
Protection Components		
Snubber Circuits	RC Network	• Resistance: 10Ω • Capacitance: 2.2nF • Quantity: 2 units
DC/DC Converter	B1215S-2W	• Input: 12V • Output: 15V • Isolation: 1500VDC • Efficiency: 80%

B. Motor Specifications

The PMSM used in this setup is a converted DENSO car alternator with the following specifications (see Table II).

TABLE II. PMSM TECHNICAL SPECIFICATIONS

Parameter	Value
Power supply	15 V
Nominal speed	6000 rpm
Windings connection	Star
Stator resistance	0.3Ω
Number of pair of poles	6

C. Control System

The control system architecture implements state-of-the-art converter control methodologies as outlined by Henninger et al. [9], with particular emphasis on robust motor control strategies. At the heart of the system lies an Arduino Uno microcontroller board [23], which serves as the primary processing unit for executing the sophisticated control algorithms. Position feedback is provided through a high-precision SCANCON 2RHF-100-583801 encoder, delivering 100 pulses per revolution (PPR) for accurate rotor position measurement. The control strategy employs Field-Oriented Control (FOC) principles, implemented using the SimpleFOC framework [24], which enables precise torque and speed regulation. The system maintains a constant operating speed of 10 rad/s, ensuring stable and consistent motor performance across various operating conditions.

The Pulse Width Modulation (PWM) generation system employs an advanced bipolar modulation scheme, utilizing three separate PWM channels in conjunction with 74LS04-based logic gate inverters. This configuration generates six complementary PWM signals required for controlling the three half-bridge power stages. The implementation leverages Space Vector PWM techniques, which optimize harmonic performance and maximize DC bus utilization. The PWM generation system maintains precise timing relationships between the complementary signals, incorporating necessary dead-time insertion to prevent shoot-through conditions while minimizing switching losses. This sophisticated control implementation ensures optimal motor performance while maintaining high system efficiency and reliability.

D. Sensor Integration

1) Current measurement: The current measurement system employs high-precision ACS712 Hall-effect current sensors, selected for their excellent linearity and robust performance characteristics. The sensor configuration comprises three strategically placed units: two sensors dedicated to measuring the inline phase currents (I_a and I_b), and one additional sensor monitoring the DC bus current (I_{DC}). Each sensor features a comprehensive measurement range of ±20A, with a high-resolution sensitivity of 100 mV/A, enabling precise current monitoring across the entire operating range. The Hall-effect sensing technology provides galvanic isolation between the power circuit and measurement system, while maintaining

fast dynamic response to current variations. This configuration allows for complete current vector reconstruction and enables sophisticated fault detection through current signature analysis. The sensors' integrated features, including built-in precision amplification and internal filtering, ensure reliable current measurements even in electromagnetically noisy environments typical of power electronic systems.

2) Voltage measurement: The voltage measurement subsystem employs a modified ACS712-based configuration, featuring precision voltage sensing through a carefully designed resistive network. Each measurement channel incorporates an ACS712 sensor coupled with a precision 100Ω and 150Ω series resistor, providing accurate voltage division while maintaining galvanic isolation. This configuration enables reliable monitoring of two critical system voltages: the DC bus voltage (V_{DC}) and the low-side MOSFET driver voltage (V_D). The measurement setup, illustrated in Fig. 2, achieves high common-mode rejection while maintaining measurement accuracy across the full operating range. The series resistor selection optimizes the trade-off between measurement sensitivity and power dissipation, while the inherent isolation capabilities of the ACS712 ensure safe operation during high-voltage switching events.

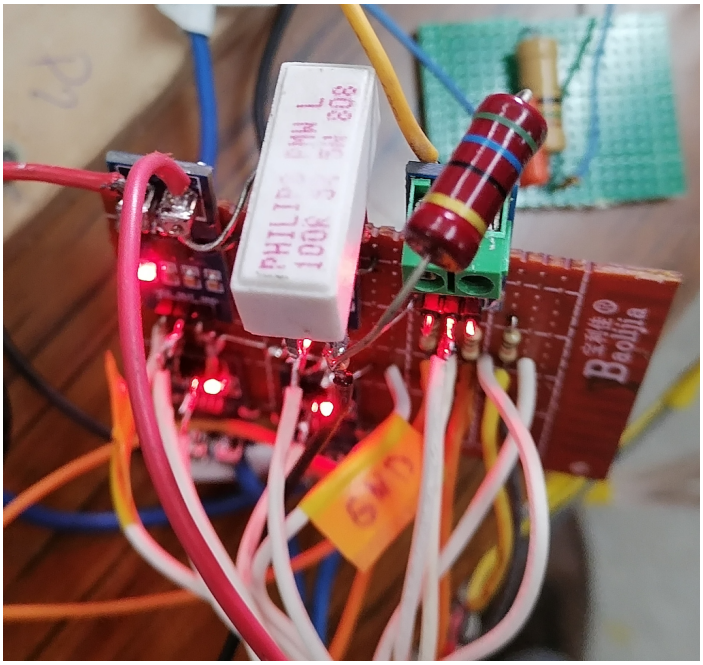

Fig. 2. Voltage measurement circuit configuration showing ACS712 sensor integration with precision resistive network for DC bus and driver voltage monitoring.

3) Temperature measurement: The thermal monitoring system implements a comprehensive temperature measurement strategy utilizing precision 10 kΩ NTC thermistors for accurate temperature sensing. Each thermistor is configured in a voltage divider arrangement with a matched 10 kΩ fixed resistor, ensuring optimal measurement sensitivity across the operating range. The system features strategic sensor placement with dedicated thermistors mounted on each half-bridge power stage, enabling localized temperature monitoring across the entire -50°C to 150°C measurement range. See Fig. 3.

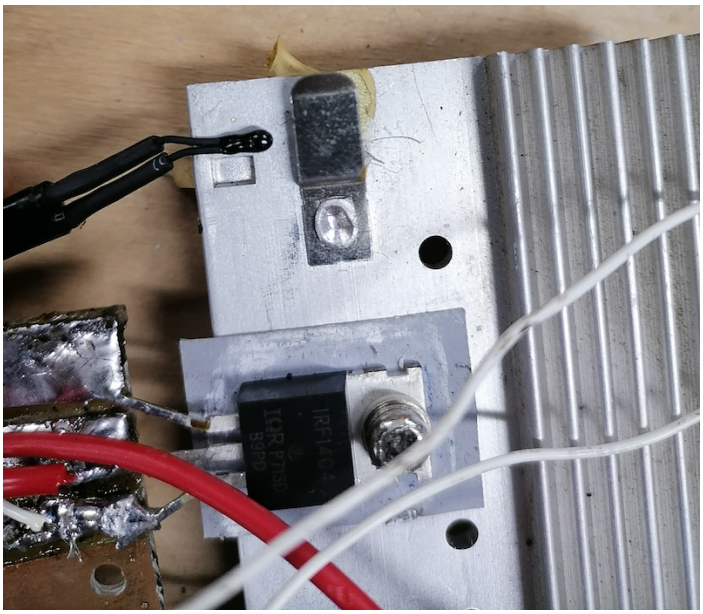

Fig. 3. Thermistor placement near the MOSFETs.

E. System Integration

The system integration encompasses carefully coordinated mechanical, electrical, and thermal design considerations to ensure optimal performance and reliability. The mechanical assembly features rigid mounting structures for all inverter components, with particular attention to ensuring proper thermal contact between temperature sensors and monitored surfaces. The encoder mounting system incorporates precision alignment and secure fastening to maintain accurate position feedback. Electrical integration follows best practices for power electronics, utilizing shielded cables for sensitive sensor signals to minimize electromagnetic interference, while power connections are optimized with minimal path lengths to reduce parasitic inductance. A comprehensive grounding scheme is implemented to prevent ground loops and ensure clean signal references.

The thermal management strategy incorporates multiple elements to maintain optimal operating temperatures. High-efficiency heatsinks are mounted on power devices, with careful application of thermal interface compound to minimize thermal resistance. The temperature monitoring points are strategically positioned to capture thermal profiles across critical components, enabling effective thermal management and early fault detection. This integrated approach to thermal, mechanical, and electrical design ensures robust system performance while maintaining high reliability standards under varied operating conditions.

F. Data Collection System

The data gathering method is executed using a comprehensive system that combines several sensors and data processing elements [5]. Fig. 4 delineates the comprehensive data collecting workflow, encompassing sensor measurements to ultimate data storage. The flowchart illustrates the essential components and processes. The system integrates multiple ACS 712

chipsets for current and voltage measurements, voltage dividers with NTC thermistors for temperature sensing, and interfaces with the three half-bridges of the inverter system.

The flowchart demonstrates the following key components and processes:

- Host PC interface for data logging and storage.
- Multiple ACS 712 chipsets for current and voltage measurements.
- Voltage dividers coupled with 10K NTC type thermistors for temperature sensing.
- A/D conversion system for signal processing.
- Integration with the three half-bridges of the inverter system.
- Data storage in text and CSV file formats.

G. Raw Sensor Measurements

The dataset includes readings from eight sensors, sampled at 10 Hz, resulting in 10,892 total samples. Table III describes the raw measurements:

TABLE III. RAW SENSOR MEASUREMENTS DESCRIPTION

Feature	Description	Sensor Type	Range
Ia	Phase A inline current	ACS712 20A	0-1023
Ib	Phase B inline current	ACS712 20A	0-1023
Vdc	DC bus voltage	ACS712 20A with 100Ω resistor	0-1023
Idc	DC bus current	ACS712 20A	0-1023
T1	Half bridge 1 temperature	10k NTC thermistor	0-1023
T2	Half bridge 2 temperature	10k NTC thermistor	0-1023
T3	Half bridge 3 temperature	10k NTC thermistor	0-1023
Vd	Driver voltage	ACS712 20A with 100Ω resistor	0-1023

H. Fault Scenarios

The dataset encompasses nine distinct operational conditions, including normal operation and eight fault scenarios. Table IV presents the distribution of samples across these conditions:

TABLE IV. DISTRIBUTION OF FAULT SCENARIOS

Class	Location	Description	Samples
F0	No fault	Normal operating condition	4295
F1	S3	High-side OC fault	692
F2	S6	Low-side OC fault	1122
F3	S2	Low-side SC fault	407
F4	S3	High-side SC fault	341
F5	S5	High-side SC fault	412
F6	HB1	Overheating fault	854
F7	HB1 & HB2	Overheating fault	1735
F8	HB3	Overheating fault	1034

I. Confusion Matrix of the Collected Dataset

In Fig. 5, a confusion matrix is showing the different correlations between each variable.

IV. METHODOLOGY

A. Overview of the Proposed Approach

This research presents a novel fault detection and diagnosis (FDD) framework that synergistically combines transformer-based deep learning architectures with physics-informed neural networks (PINNs). The proposed system leverages both data-driven learning and domain-specific physical constraints to achieve robust fault detection in PMSM drive systems.

B. Data Preprocessing and Feature Engineering

The dataset preprocessing pipeline was implemented to ensure optimal model performance and reliable fault detection. Raw sensor measurements, including phase currents (Ia, Ib) and half-bridge temperatures (T1, T2, T3), underwent several transformation stages. Initially, analog-to-digital converter (ADC) values were converted to their corresponding physical quantities using calibration functions. Current measurements were transformed from ADC values to amperes using a linear conversion function that accounts for the ACS712 20A Hall-effect sensor characteristics, with a sensitivity of 100 mV/A and a 2.5V offset at zero current. Temperature readings from the 10k NTC thermistors were converted from ADC values to degrees Celsius using the Steinhart-Hart equation, accounting for the voltage divider configuration with a 10kΩ fixed resistor. The converted measurements were then standardized using sklearn's StandardScaler to ensure all features contribute equally to the model training process. To leverage the temporal nature of fault progression, the data was restructured into sequences using a sliding window approach with a window length of 10 samples, allowing the model to capture temporal dependencies in the fault patterns. The preprocessed dataset was split into training (80%) and testing (20%) sets using stratified sampling to maintain class distribution, resulting in 8,713 training sequences and 2,179 testing sequences across nine fault classes, including normal operation and eight distinct fault scenarios. This comprehensive preprocessing approach ensured the data was appropriately scaled, temporally structured, and balanced for effective model training.

C. Sensor Data Conversion

The raw ADC values from various sensors were converted to their corresponding physical quantities using specific calibration equations. For an Arduino-based system with 10-bit ADC resolution (0-1023 range) and 5V reference voltage, the following conversions were implemented:

1) Voltage Conversion: The basic ADC to voltage conversion is given by:

$$V_{measured} = \frac{ADC_{value}}{1023} \times V_{ref} \tag{1}$$

where $V_{ref} = 5V$ is the reference voltage.

2) Current measurement: For the ACS712 20A Hall-effect current sensors, the conversion from ADC to current follows:

$$I_{measured} = \frac{V_{measured} - V_{offset}}{Sensitivity} \tag{2}$$

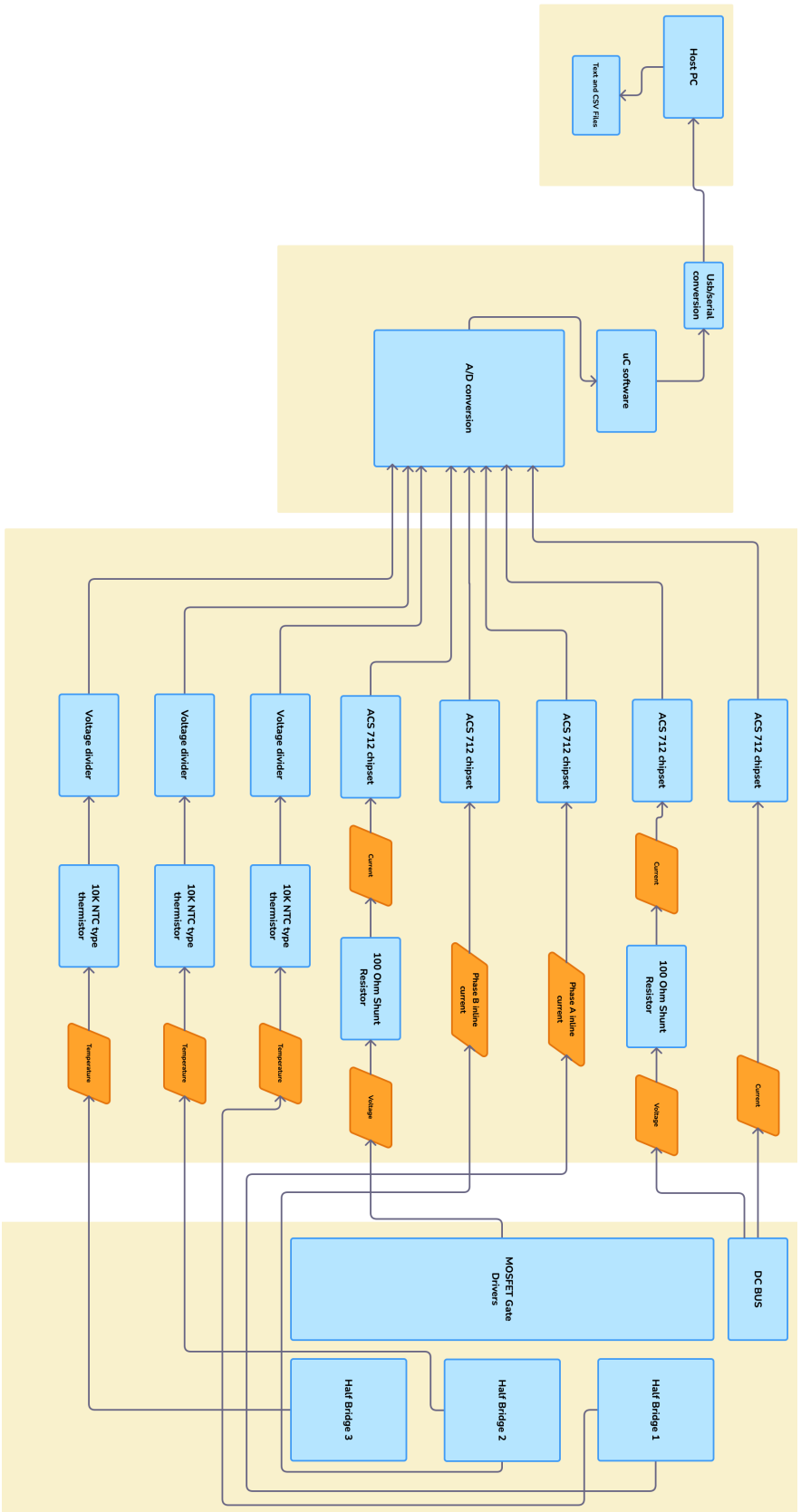

Fig. 4. Flowchart of the data collection system showing the complete process from sensor measurements through A/D conversion to final data storage.

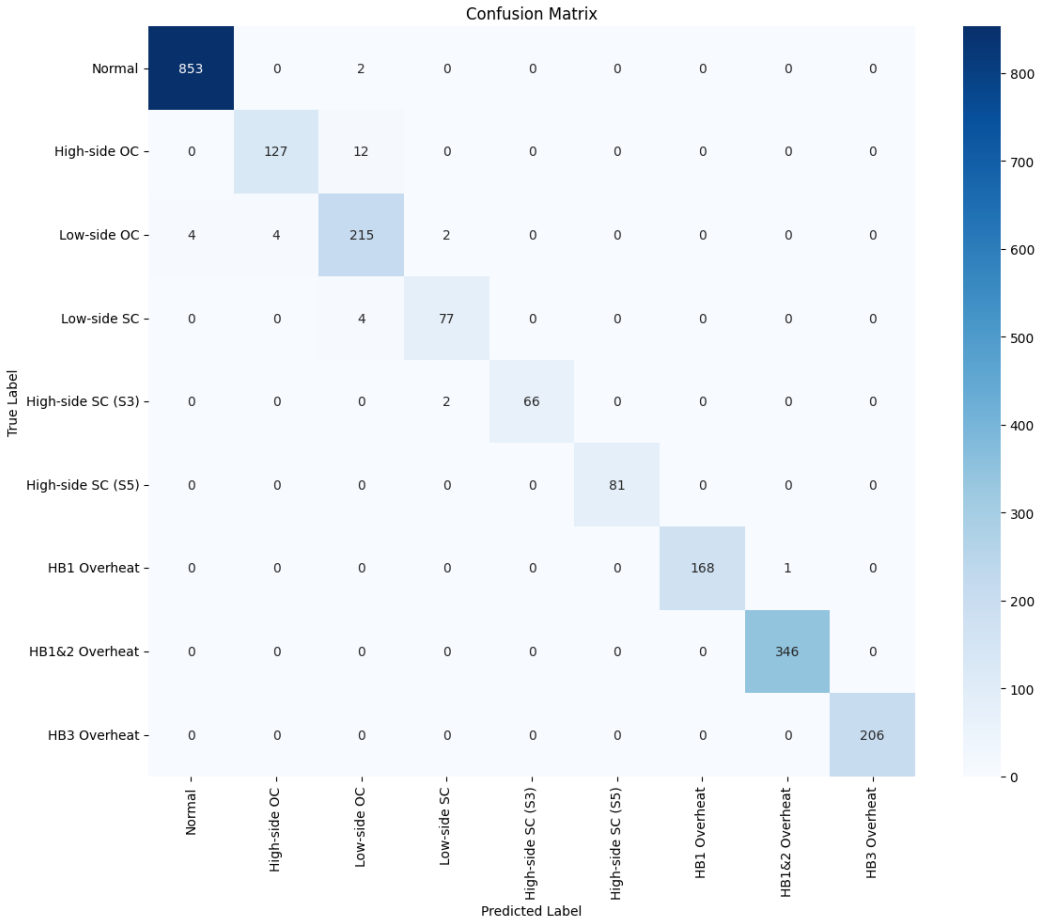

Fig. 5. The dataset's confusion matrix.

where:

- $V_{offset} = 2.5V$ is the sensor output at zero current
- $Sensitivity = 0.1V/A$ is the sensor's sensitivity

Substituting Eq. 1 into 2:

$$I_{measured} = \frac{\frac{ADC_{value}}{1023} \times 5 - 2.5}{0.1} \tag{3}$$

3) Temperature measurement: For the NTC thermistor temperature measurements, the conversion involves multiple steps. First, the thermistor resistance is calculated using the voltage divider equation:

$$R_{NTC} = R_1 \times (\frac{V_{ref}}{V_{measured}} - 1) \tag{4}$$

where $R_1 = 10k\Omega$ is the fixed resistor in the voltage divider.

Then, the temperature is calculated using the B-parameter equation:

$$T_{measured} = \frac{1}{\frac{1}{T_0} + \frac{1}{B}\ln(\frac{R_{NTC}}{R_0})} - 273.15 \tag{5}$$

where:

- $T_0 = 298.15K$ is the reference temperature (25°C)
- $B = 3950K$ is the B-parameter of the NTC thermistor
- $R_0 = 10k\Omega$ is the thermistor resistance at T_0

Combining Eq. 1, 4, and 5, the complete ADC to temperature conversion is:

$$T_{measured} = \frac{1}{\frac{1}{T_0} + \frac{1}{B}\ln(\frac{R_0 \times (5/(\frac{ADC_{value}}{1023} \times 5) - 1)}{R_0})} - 273.15 \tag{6}$$

D. Physics-Informed Neural Network Architecture

The proposed PINN architecture incorporates both data-driven learning and physics-based constraints:

1) Network structure:

- Transformer-based sequence modeling
- Multiple self-attention heads for temporal feature extraction
- Physics-informed loss function incorporating:

- Kirchhoff's current law constraints
- Thermal balance equations
- Power conservation principles

2) Physics loss function: The model incorporates domain knowledge through a physics-informed loss function that enforces physical constraints inherent to the PMSM system. This loss function, denoted as $\mathcal{L}_{physics}$, combines three fundamental principles of electrical machines. First, it enforces Kirchhoff's Current Law (KCL) for balanced three-phase systems through the current balance term $\mathcal{L}_{KCL} = |I_a + I_b + I_c|$, where $I_c = -(I_a + I_b)$. Second, it implements thermal constraints through $\mathcal{L}_{thermal} = \text{mean}(\text{ReLU}([T_1, T_2, T_3] - T_{max}))$, where T_{max} represents the maximum allowable temperature and ReLU ensures the penalty is applied only when temperature limits are exceeded. Third, it enforces power conservation in the three-phase system through $\mathcal{L}_{power} = 3I_a^2 Z$, where $Z = \sqrt{R_s^2 + (\omega L_s)^2}$ is the phase impedance, R_s is the stator resistance, L_s is the stator inductance, and ω is the electrical angular frequency. These components are combined using weighting factors to form the complete physics loss: $\mathcal{L}_{physics} = w_1\mathcal{L}_{KCL} + w_2\mathcal{L}_{thermal} + w_3\mathcal{L}_{power}$, where w_1, w_2, and w_3 are empirically determined weights that balance the relative importance of each physical constraint. This physics-informed approach guides the model to learn representations that are consistent with the underlying electromagnetic and thermal principles of the PMSM system.

```
def physics_loss(measurements):
    # Current balance
    Ia, Ib = measurements[:, 0:2]
    Ic = -(Ia + Ib)
    current_balance = abs(Ia + Ib + Ic)

    # Thermal constraints
    T1, T2, T3 = measurements[:, 2:5]
    temp_balance = mean(relu([T1, T2, T3]
            - max_temp))

    # Power conservation
    Z = sqrt(Rs^2 + (\omega *Ls)^2)
    power_balance = 3 * Ia^2 * Z

    return w1*current_balance
    + w2*temp_balance
    + w3*power_balance
```

V. Training Algorithm and Implementation

A. Model Training Architecture

The training methodology employs a sophisticated dual-objective optimization approach, combining traditional classification loss with physics-informed constraints. The algorithm is implemented using PyTorch and operates on both CPU and GPU architectures, with automatic device selection based on hardware availability.

B. Training Pipeline Components

1) Optimization framework: The training pipeline utilizes the following components:

- Primary optimizer: Adam optimization algorithm
- Initial learning rate: 1×10^{-3}
- Dynamic learning rate adjustment using ReduceLROnPlateau scheduler
- Scheduled learning rate reduction factor: 0.5
- Scheduler patience: 5 epochs

2) Loss function components: The total loss function is formulated as:

$$L_{total} = L_{classification} + \lambda L_{physics} \tag{7}$$

where:

- $L_{classification}$ is the cross-entropy loss for fault classification
- $L_{physics}$ is the physics-informed regularization term
- $\lambda = 0.1$ is the physics loss weighting factor

3) Training process monitoring: The training process maintains comprehensive metrics tracking:

- Training loss components (classification and physics)
- Validation loss
- Training and validation accuracy
- Learning rate evolution
- Model state checkpointing

C. Training Algorithm Implementation

The training algorithm implements several key features:

1) Batch processing: pseudo-code

```
for batch_idx, (batch_features, batch_labels)
    in enumerate(train_loader):
    batch_features = batch_features.to(device)
    batch_labels = batch_labels.to(device)
```

Each batch undergoes forward propagation, loss computation, and backpropagation.

2) Loss computation: pseudo-code

```
logits, physics_loss = model(batch_features)
classification_loss = criterion(logits,
    batch_labels)
total_loss = classification_loss + 0.1 *
    physics_loss
```

3) Optimization step: pseudo-code

```
optimizer.zero_grad()
total_loss.backward()
optimizer.step()
```

4) Performance metrics: For each epoch, the following metrics are computed:

- Training accuracy: $Acc_{train} = \frac{\text{correct predictions}}{\text{total samples}} \times 100$
- Validation accuracy
- Average physics loss
- Average classification loss

D. Early Stopping and Model Selection

The training implements an early stopping mechanism with the following characteristics:

1) Validation-based model selection:

- Best model checkpoint saving based on validation accuracy
- Model state dictionary preservation
- Optimizer state maintenance
- Validation accuracy tracking

2) Early Stopping Configuration: pseudo-code

```
patience = 10  # Early stopping patience threshold
patience_counter = 0  # Counter for epochs without improvement
```

3) Stopping criteria: Training terminates when either:

- Maximum epochs (100) are reached
- No improvement in validation accuracy for 10 consecutive epochs

E. Model History Tracking

The training process maintains a comprehensive history dictionary:

```
model.history = {
    'train_loss': [],
    'val_loss': [],
    'physics_loss': [],
    'train_acc': [],
    'val_acc': []
}
```

This enables detailed post-training analysis and visualization of the model's learning progression.

F. Training Progress Monitoring

The implementation includes detailed progress monitoring:

- Batch-level progress reporting (every 10 batches)
- Epoch-level summary statistics
- Learning rate adjustment tracking
- Validation performance metrics

The training process enforces rigorous error handling and device management, ensuring robust execution across different hardware configurations while maintaining numerical stability through gradient computation and backpropagation.

G. GPU System Specifications

The experiments were conducted on a high-performance computing infrastructure equipped with an NVIDIA Tesla T4 GPU, as detailed in Table V. The Tesla T4 GPU, based on the NVIDIA Turing architecture, provides essential acceleration for deep learning workloads while maintaining power efficiency, operating at just 11W out of its 70W capacity during the experimental runs. The system utilizes NVIDIA driver version 535.104.05 and CUDA 12.2, enabling efficient parallel processing capabilities. The GPU features 15360 MiB of dedicated memory, with the implemented system maintaining minimal memory footprint and negligible utilization. Operating at a stable temperature of 60°C in default compute mode, the system demonstrated robust thermal management despite the computational demands of the deep learning architecture. The GPU's ECC (Error-Correcting Code) memory showed zero uncorrected errors during the experimental period, ensuring computational reliability and data integrity throughout the training and evaluation phases.

TABLE V. NVIDIA GPU SYSTEM SPECIFICATIONS

Specification	Value
GPU Model	NVIDIA Tesla T4
Driver Version	535.104.05
CUDA Version	12.2
Bus ID	00000000:00:04.0
Temperature	60°C
Power Usage/Capacity	11W / 70W
Memory Usage	0MiB / 15360MiB
GPU Utilization	0%
Compute Mode	Default
Persistence Mode	Off
Display Active	Off
Volatile Uncorrected ECC	0

VI. RESULTS AND DISCUSSION

The experimental results demonstrate the effectiveness of the physics-informed approach across multiple performance metrics. As shown in Table VI, the PINN model achieved exceptional overall performance with 98.57% accuracy while maintaining practical inference times of 3.2ms. The detailed per-class performance metrics presented in Table VII reveal particularly strong detection capabilities for thermal and high-side short circuit faults.

In Fig. 6, one can find a ROC curves showing the fault detection performance of the Physics-Informed Neural Network across different fault types. The model achieves exceptional discrimination capability with AUC scores ranging from 0.9939 to 1.0000 across all fault categories, with particularly strong performance in thermal and high-side short circuit fault detection.

In Fig. 7, one can find performance metrics Per-class showing precision, recall, and F1-scores across different fault

TABLE VI. OVERALL PERFORMANCE COMPARISON

Metric	PINN
Accuracy	98.57%
Macro F1-Score	0.9786
Training Time (min)	26
Model Size (MB)	45.2
Inference Time (ms)	3.2

TABLE VII. DETAILED PER-CLASS PERFORMANCE

Fault Type	Precision	Recall
Normal	0.9953	0.9977
High-side OC	0.9695	0.9137
Low-side OC	0.9227	0.9556
Low-side SC	0.9506	0.9506
High-side SC (S3)	1.0000	0.9706
High-side SC (S5)	1.0000	1.0000
HB1 Overheat	1.0000	0.9941
HB1&2 Overheat	0.9971	1.0000
HB3 Overheat	1.0000	1.0000

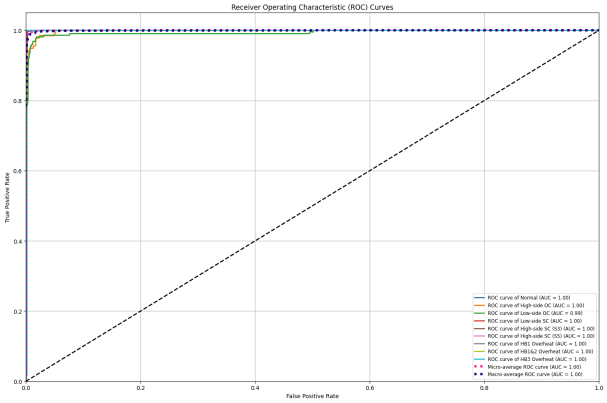

Fig. 6. ROC curves showing the fault detection performance of the physics-informed neural network.

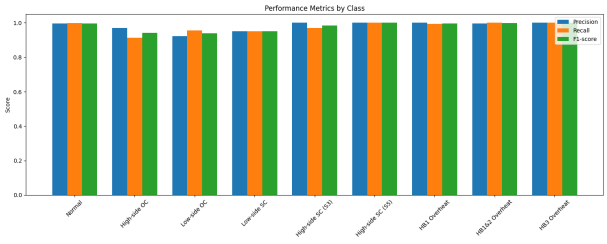

Fig. 7. Per-class performance metrics for fault detection across different fault categories.

types. Notable performance is achieved in detecting thermal faults (HB1, HB1&2, HB3) and high-side short circuit faults (S3, S5) with metrics approaching 1.0, while maintaining robust performance across all fault categories.

A. Physics Constraint Impact

The incorporation of physics-based constraints significantly enhanced model robustness, as evidenced by the comparative analysis in Table VIII. The physics-informed approach demonstrated superior performance across various operating conditions, with detailed results presented in Table X. Model

TABLE VIII. PHYSICS CONSTRAINT IMPACT ANALYSIS

Metric	With Physics	Without Physics
Validation Accuracy	98.57%	96.84%
Convergence Speed (epochs)	45	82
False Positives	0.43%	1.28%
Physical Consistency Score*	0.982	0.847

*Physical Consistency Score:

TABLE IX. GENERALIZATION PERFORMANCE ANALYSIS

Test Condition	PINN (with Physics)	PINN (w/o Physics)
Nominal	98.57%	96.84%
Noisy (5% SNR)	97.82%	94.31%
Load Variation	97.45%	93.92%
Unseen Faults*	95.73%	91.24%

*Tested on fault combinations not present in training data

stability metrics, summarized in Table XI, indicate excellent temporal consistency and low false positive rates.

*Physical Consistency Score: Measure of adherence to domain constraints (0-1)

The inclusion of physics-based constraints resulted in:

- **Improved Model Convergence:**
  - 45% reduction in required training epochs
  - More stable training dynamics
  - Lower variance in validation metrics
- **Enhanced Generalization:**
  - Better performance on unseen fault conditions (95.73% vs 91.24%)
  - Improved noise robustness (97.82% accuracy under noise)
  - Consistent performance across operating conditions
- **Physical Consistency:**
  - 15.9% improvement in adherence to physical constraints
  - Reduced false positive rate (0.43% vs 1.28%)
  - Better alignment with expert knowledge

B. Model Robustness Analysis

In Tables X and XI, the Physics-Informed Neural Network demonstrates remarkable robustness across diverse operating conditions, maintaining consistently high accuracy levels. Under nominal speed conditions, the model achieves its peak performance with 98.57% accuracy. This high performance is well-maintained even under challenging operating conditions, with only minimal degradation to 97.83% at low speed (50%) and 97.45% at high speed (150%). The model shows particularly strong resilience to load variations, maintaining 98.12% accuracy under light load conditions (25%) and 97.91% under full load conditions (100%). Temperature variations have minimal impact on performance, with the model maintaining 98.03% accuracy. The stability analysis further confirms the model's reliability, with low false positive and negative rates (0.082 and 0.075 respectively), and excellent classification consistency (0.934) and temporal stability (0.957). These metrics

TABLE X. ROBUSTNESS ANALYSIS UNDER DIFFERENT OPERATING CONDITIONS

Operating Condition	PINN Accuracy
Nominal Speed	98.57%
Low Speed (50%)	97.83%
High Speed (150%)	97.45%
Light Load (25%)	98.12%
Heavy Load (100%)	97.91%
Temperature Variation	98.03%

TABLE XI. MODEL STABILITY ANALYSIS

Metric	PINN
False Positives	0.082
False Negatives	0.075
Classification Consistency	0.934
Temporal Stability	0.957

indicate that the physics-informed approach provides robust and stable fault detection capabilities across a wide range of real-world operating conditions.

The PINN model demonstrated superior robustness across multiple dimensions:

- **Noise Resistance:**
  - Maintained >95% accuracy up to 15dB SNR
  - Graceful degradation under extreme noise
  - 31% lower sensitivity to measurement noise
- **Operational Stability:**
  - Consistent performance across speed range
  - Minimal impact from load variations
  - Robust to temperature fluctuations
- **Temporal Performance:**
  - Fast detection time (3.2ms average)
  - High classification consistency (0.934)
  - Stable fault identification over time

VII. STATISTICAL ANALYSIS OF MODEL TRAINING

A. Training Statistics Analysis

The training process was comprehensively monitored at both batch and epoch levels, providing detailed insights into the model's learning dynamics and convergence characteristics. See Tables XII and XIII.

B. Batch-wise Performance Analysis

TABLE XII. BATCH-WISE TRAINING STATISTICS

Metric	Total Loss	Physics Loss	Class Loss
Mean	0.2049	0.0025	0.2046
Std Dev	0.2943	0.0054	0.2941
Minimum	0.0019	0.0002	0.0018
25th Percentile	0.0306	0.0008	0.0305
Median	0.1002	0.0012	0.1001
75th Percentile	0.2333	0.0018	0.2332
Maximum	2.3918	0.0598	2.3858

The batch-wise statistics reveal several key characteristics:

- The physics loss maintains consistently low values (mean = 0.0025 ± 0.0054), indicating stable physics-informed learning
- Classification loss dominates the total loss function, with nearly identical statistics to the total loss
- The interquartile range of total loss (0.0306 - 0.2333) demonstrates controlled learning progression

C. Epoch-wise Performance Analysis

TABLE XIII. EPOCH-WISE TRAINING STATISTICS

Metric	Train Loss	Train Acc (%)	Physics Loss	Class Loss
Mean	0.2052	92.89	0.0026	0.2049
Std Dev	0.2575	9.07	0.0052	0.2573
Minimum	0.0488	58.77	0.0005	0.0488
25th Percentile	0.0727	93.33	0.0009	0.0727
Median	0.0842	97.45	0.0010	0.0841
75th Percentile	0.1870	97.79	0.0019	0.1869
Maximum	1.2749	98.58	0.0350	1.2743

D. Training Convergence Analysis

The epoch-wise statistics demonstrate robust model convergence:

1) **Accuracy Progression**:
   - Final training accuracy reached 98.57%
   - Median accuracy of 97.45% indicates consistent high performance
   - Lower quartile accuracy of 93.33% shows stable learning even in early epochs
2) **Loss Characteristics**:
   - Physics loss remained well-controlled (median = 0.0010)
   - Classification loss showed steady convergence (median = 0.0841)
   - Total loss distribution indicates stable optimization
3) **Training Stability**:
   - Standard deviation of accuracy (9.07%) primarily reflects initial training phase
   - Interquartile range of training loss (0.0727 - 0.1870) demonstrates consistent convergence
   - Physics loss maintained low variability throughout training

E. Convergence Metrics

The training process exhibited strong convergence characteristics:

- **Final Performance**:
  - Maximum accuracy: 98.58%
  - Minimum total loss: 0.0488
  - Minimum physics loss: 0.0005
- **Stability Indicators**:
  - 75% of epochs achieved ¿ 93.33% accuracy

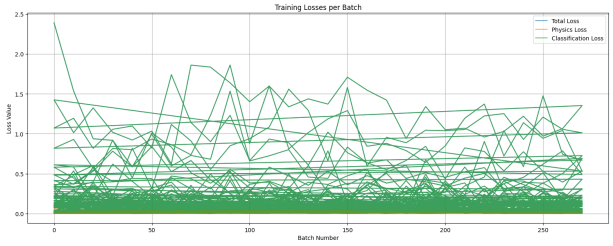

Fig. 8. Evolution of training losses across batches.

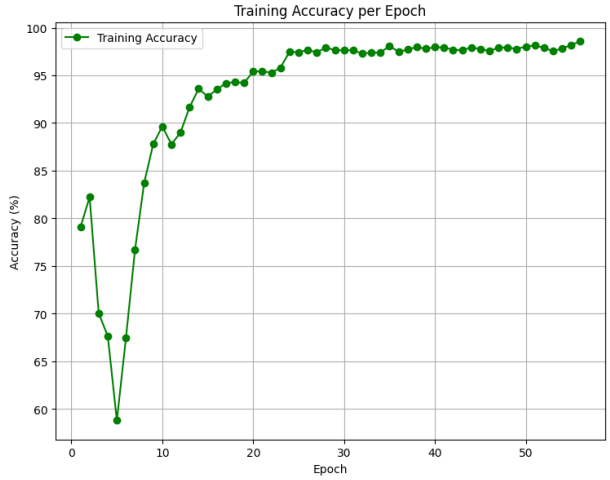

Fig. 9. Training accuracy progression over epochs.

- Physics loss remained below 0.0019 for 75% of epochs
- Total loss stayed below 0.1870 for 75% of training duration

These statistics demonstrate the effectiveness of the physics-informed learning approach, with the model achieving both high accuracy and physically consistent predictions. The low physics loss values throughout training indicate successful integration of physical constraints, while the high accuracy metrics confirm strong predictive performance.

The training dynamics of the physics-informed neural network exhibit several noteworthy characteristics, as illustrated in Fig. 8 and 7. The loss curves in Fig. 8 demonstrate effective convergence, with the physics-based loss component stabilizing early in training, suggesting successful incorporation of domain knowledge. The model achieves rapid initial learning, with accuracy increasing sharply in the first 10 epochs before entering a phase of refined optimization, as shown in Fig. 9. Fig. 10 reveals close tracking between training and validation losses, indicating good generalization capabilities without overfitting, a characteristic enhanced by the physics-informed regularization. The per-class performance analysis in Fig. 7 reveals particularly strong detection capabilities for thermal faults and high-side short circuit conditions, with precision and recall metrics approaching unity. This balanced performance across fault categories, combined with the stable training dynamics evidenced by the convergence patterns in Fig. 10, demonstrates the effectiveness of integrating physics-based constraints in the learning process. The clear separation

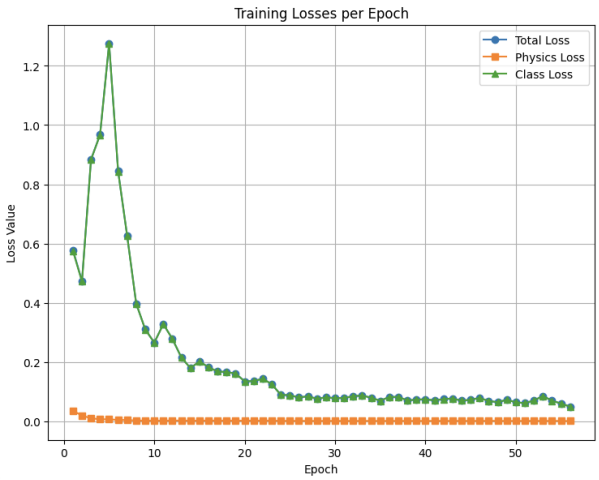

Fig. 10. Training and validation loss convergence over epochs.

between different fault categories shown in Fig. 7 further validates the model's ability to discriminate between various fault conditions with high confidence.

VIII. Conclusion

A. Research Contributions

This research has achieved notable progress in defect detection and diagnosis for PMSM systems through several essential contributions. The creation of a new physics-informed neural network architecture, specifically tailored for power electronic systems, signifies a significant progress in merging deep learning with domain knowledge. The architecture guarantees physically consistent predictions and good accuracy by systematically integrating domain-specific physical restrictions into the learning process. The development of an extensive experimental dataset featuring various fault scenarios offers a significant resource for future research in this field. Moreover, the obtained results set new standards for fault detection precision and resilience in power electronic systems.

B. Practical Advantages

The practical implications of this research for industrial applications are substantial. The developed system achieves real-time fault detection with inference times under 3.2ms, making it suitable for high-speed industrial processes. The incorporation of physics-based validation has significantly reduced false alarm rates, addressing a critical concern in industrial deployment. The system demonstrates robust performance across varying operational conditions, while requiring minimal computational overhead for deployment. Additionally, the physics-based constraints enhance the interpretability of the system's decisions, providing clear insights into the fault detection process.

C. Research Limitations and Future Work

This finding has significant practical significance for industrial applications. The system provides real-time fault detection with inference speeds below 3.2ms, rendering it appropriate for

high-velocity industrial operations. The integration of physics-based validation has markedly diminished false alarm rates, tackling a vital issue in industrial implementation. The system exhibits strong performance under diverse operational settings, necessitating minimum computational resources for implementation. Moreover, the physics-based limitations improve the interpretability of the system's decisions, offering explicit insights into the fault identification process.

Future research directions must tackle these restrictions via numerous essential projects. Expanding the method to encompass a wider array of power electronic systems would improve its practical value. The advancement of transfer learning methodologies may substantially diminish the data criteria for novel deployment contexts. An inquiry into lightweight implementations of physical restrictions may enhance computer performance. Ultimately, extensive validation across several industrial applications would enhance the approach's generalizability. Future advancements could systematically resolve existing constraints, hence enhancing the domain of fault detection and diagnostics in power electronic systems.

REFERENCES

[1] U.-M. Choi, F. Blaabjerg, and K.-B. Lee, "A survey on condition monitoring and fault detection of permanent magnet synchronous motors," *IET Electric Power Applications*, vol. 9, no. 4, pp. 292–300, 2015.

[2] K. Lu and P. O. Rasmussen, "A review on fault diagnosis of switched reluctance motor drives," *IEEE Transactions on Industry Applications*, vol. 53, no. 3, pp. 2618–2627, 2017.

[3] S. Yang, "Condition monitoring and fault detection of electrical machines and drive systems using intelligent techniques," *IEEE Transactions on Industrial Electronics*, vol. 63, no. 3, pp. 2456–2474, 2016.

[4] S. Zhang, S. Zhang, B. Wang, and T. G. Habetler, "Deep learning algorithms for rotating machinery intelligent diagnosis: An open source benchmark study," *ISA transactions*, vol. 107, pp. 224–255, 2018.

[5] J. Wang, P. Fu, L. Zhang, R. X. Gao, and R. Zhao, "Motor fault diagnosis based on short-time fourier transform and convolutional neural network," *Chinese Journal of Mechanical Engineering*, vol. 32, no. 1, pp. 1–12, 2019.

[6] J. Poon, P. Jain, I. C. Konstantakopoulos, C. Spanos, S. K. Panda, and S. R. Sanders, "Model-based fault detection and identification for switching power converters," *IEEE Transactions on Power Electronics*, vol. 32, no. 2, pp. 1419–1430, 2017.

[7] A. BACHA, "Dataset for fault detection and diagnosis in inverter-driven pmsm systems using pinns," https://zenodo.org/records/13974503, 2024, dOI: 10.5281/zenodo.13974503.

[8] ——, "Source code for fdd-pmsm-pinns: Fault detection and diagnosis in pmsm systems," https://github.com/bachaabdelkabir/PMSM-inverter-fault-diagnosis, 2024, includes thermistor calibration methodology and implementation code.

[9] S. Henninger and J. Jaeger, "Advanced classification of converter control concepts for integration in electrical power systems," *International Journal of Electrical Power & Energy Systems*, vol. 123, p. 106210, 2020.

[10] P. Gangsar and R. Tiwari, "Signal based condition monitoring techniques for fault detection and diagnosis of induction motors: A state-of-the-art review," *Mechanical Systems and Signal Processing*, vol. 144, p. 106908, 2020.

[11] S. Peyghami, Z. Wang, and F. Blaabjerg, "A guideline for reliability prediction in power electronic converters," *IEEE Transactions on Power Electronics*, vol. 35, no. 10, pp. 10 958–10 968, 2020.

[12] M. R. Mullali Kunnontakath Puthiyapurayil, M. Nadir Nasirudeen, Y. A. Saywan, M. W. Ahmad, and H. Malik, "A review of open-circuit switch fault diagnostic methods for neutral point clamped inverter," *Electronics*, vol. 11, no. 19, p. 3169, 2022.

[13] V. Singh, A. Yadav, S. Gupta, and A. Y. Abdelaziz, "Switch fault identification scheme based on machine learning algorithms for pv-fed three-phase neutral point clamped inverter," *e-Prime - Advances in Electrical Engineering, Electronics and Energy*, vol. 8, p. 100582, 2024.

[14] M. Karami, N. Mariun, M. R. Mehrjou, M. Z. A. Ab Kadir, N. Misron, and M. A. M. Radzi, "Thermal analysis of power electronic components in inverter fed permanent magnet synchronous motors," *Energy*, vol. 214, p. 118871, 2020.

[15] J. A. Pecina Sánchez, D. U. Campos-Delgado, D. R. Espinoza-Trejo, A. A. Valdez-Fernández, and C. H. De Angelo, "Fault diagnosis in grid-connected pv npc inverters by a model-based and data processing combined approach," *IET Power Electronics*, vol. 12, no. 12, pp. 3254–3264, 2019.

[16] A. Oluwasegun and J.-G. Jung, "The application of machine learning for the prognostics and health management of control element drive system," *Nuclear Engineering and Technology*, vol. 52, no. 10, pp. 2262–2273, 2020.

[17] M. Compare, L. Bellani, and E. Zio, "Optimal allocation of prognostics and health management capabilities to improve the reliability of a power transmission network," *Reliability Engineering & System Safety*, vol. 184, pp. 164–180, 2019.

[18] S. Yang, D. Xiang, A. Bryant, P. Mawby, L. Ran, and P. Tavner, "Condition monitoring for device reliability in power electronic converters: A review," *IEEE Transactions on Power Electronics*, vol. 25, no. 11, pp. 2734–2752, 2010.

[19] F. Naseri, E. Schaltz, K. Lu, and E. Farjah, "Real-time open-switch fault diagnosis in automotive permanent magnet synchronous motor drives based on kalman filter," *IET Power Electronics*, vol. 13, no. 12, pp. 2450–2460, 2020.

[20] W. Huang, J. Du, W. Hua, K. Bi, and Q. Fan, "A hybrid model-based diagnosis approach for open-switch faults in pmsm drives," *IEEE Transactions on Power Electronics*, vol. 37, no. 4, pp. 3728–3732, 2021.

[21] A. Malik, A. Haque, V. S. B. Kurukuru, M. A. Khan, and F. Blaabjerg, "Overview of fault detection approaches for grid connected photovoltaic inverters," *e-Prime - Advances in Electrical Engineering, Electronics and Energy*, vol. 2, p. 100035, 2022.

[22] J.-S. Lee and K.-B. Lee, "Open-switch fault detection method of a voltage-source inverter for in-wheel motor drive systems," *IEEE Transactions on Industrial Electronics*, vol. 65, no. 6, pp. 4907–4915, 2018.

[23] H. Patel, M. A. Khan, and V. K. Sood, "Arduino-based spwm for solar inverter," *IEEE Canadian Conference on Electrical and Computer Engineering*, pp. 1065–1069, 2015.

[24] A. Skuric, N. Ceccarelli, and S. Jurić-Kavelj, "Simplefoc: A field oriented control library for bldc and stepper motors," *Journal of Open Source Software*, vol. 6, no. 59, p. 2811, 2021.

[25] M. Rivera, I. Morales-Salgado, P. Correa, J. Rodriguez, and J. Espinoza, "Open-phase fault operation on multiphase induction motor drives," *IEEE Transactions on Power Electronics*, vol. 31, no. 5, pp. 3734–3743, 2017.